A combined experimental/numerical investigation on hygrothermal aging of fiber-reinforced composites

Rocha, I. B.C.M.; van der Meer, F. P.; Raijmaekers, S.; Lahuerta, F.; Nijssen, R. P.L.; Mikkelsen, L. P.; Sluys, L. J.

DOI
10.1016/j.euromechsol.2018.10.003

Publication date
2019

Document Version
Accepted author manuscript

Published in
European Journal of Mechanics, A/Solids

Citation (APA)
Rocha, I. B. C. M., van der Meer, F. P., Raijmaekers, S., Lahuerta, F., Nijssen, R. P. L., Mikkelsen, L. P., & Sluys, L. J. (2019). A combined experimental/numerical investigation on hygrothermal aging of fiber-reinforced composites. *European Journal of Mechanics, A/Solids*, *73*, 407-419. https://doi.org/10.1016/j.euromechsol.2018.10.003

A combined experimental/numerical investigation on hygrothermal aging of fiber-reinforced composites

I. B. C. M. Rocha[1,2], F. P. van der Meer[2], S. Raijmaekers[1], F. Lahuerta[1], R. P. L. Nijssen[1], L. P. Mikkelsen[3], and L. J. Sluys[2]

[1]Knowledge Centre WMC, Kluisgat 5, 1771MV Wieringerwerf, The Netherlands
[2]Delft University of Technology, Faculty of Civil Engineering and Geosciences, P.O. Box 5048, 2600GA Delft, The Netherlands
[3]Technical University of Denmark, Department of Wind Energy, Composites and Materials Mechanics, DTU Risø Campus, 4000 Roskilde, Denmark

Abstract

This work investigates hygrothermal aging degradation of unidirectional glass/epoxy composite specimens through a combination of experiments and numerical modeling. Aging is performed through immersion in demineralized water. Interlaminar shear testes are performed after multiple conditioning times and after single immersion/redrying cycles. Degradation of the fiber-matrix interface is estimated using single-fiber fragmentation tests and reverse modeling combining analytical and numerical models. A fractographic analysis of specimens aged at $50\,^{\circ}\mathrm{C}$ and $65\,^{\circ}\mathrm{C}$ is performed through X-ray computed tomography. The aging process is modeled using a numerical framework combining a diffusion analysis with a concurrent multiscale model with embedded hyper-reduced micromodels. At the microscale, a pressure-dependent viscoelastic/viscoplastic model with damage is used for the resin and fiber-matrix debonding is modeled with a cohesive-zone model including friction. A comparison between numerical and experimental results is performed.

Keywords: Fiber-reinforced composites, multiscale analysis, reduced-order modeling

1 Introduction

Fiber-reinforced composite materials feature an intrinsically multiscale behavior. Owing to their complex microstructures, predicting failure in composite materials requires knowledge on a number of microscopic failure mechanisms and on their highly nonlinear interactions leading up to macroscopic failure [1, 2, 3].

Complexity is further increased when the interaction between the material and its service environment is taken into account. In the particular case of hygrothermal aging, a combination of high temperatures and moisture ingression, processes such as differential swelling, plasticization and hydrolysis can severely impact the mechanical performance of the composite material [4, 5, 6]. Besides affecting each microscopic material component differently, these degradation processes may act on different time scales and be either reversible or irreversible [7].

Research on hygrothermal aging of fiber-reinforced composites has often focused on macroscopic experiments which, although providing valuable information on material degradation at scales closer to the ones used in structural design, offer limited insight in the underlying microscopic aging mechanisms [8, 9, 10, 11]. A number of authors [12, 1, 13] attempt to further the understanding of these mechanisms through a combination of micromechanical tests, novel micro-

and nanoscale observation techniques and high-fidelity numerical modeling, leading to more realistic predictions of composite material durability.

Micromechanical modeling allows for fibers, matrix and interfaces to be explicitly modeled and specialized constitutive models to be employed for each of them. This enables capturing complex material behavior such as viscous effects in the resin [14, 15] and debonding with friction at interfaces [1, 16]. Macroscopic behavior can in turn be obtained through a bottom-up numerical homogenization procedure [3, 1] after which the micromodel is substituted by a calibrated mesoscale model. Alternatively, both scales can be treated concurrently through computational homogenization (FE^2) [17, 18, 19]. This approach allows for realistic modeling of macroscopic structures with non-uniform degradation states without any mesoscale constitutive assumptions. However, as FE^2 involves the concurrent modeling of multiple microscopic domains, gains in fidelity and generality come at the cost of computational efficiency. In order to circumvent this drawback, reduced-order modeling techniques can be used to accelerate the computation of the micromodels [20, 21, 22].

This paper presents a combined experimental and numerical investigation on hygrothermal aging of a glass/epoxy composite system. The work builds upon previous experimental [7] and numerical [18] studies performed by the authors, combining them and including a number of relevant improvements. For the experimental part, a new set of mechanical tests is performed on purely unidirectional short-beam specimens aged in demineralized water at $50\,^{\circ}\mathrm{C}$ for different durations in order to track the evolution of material degradation, including tests on samples redried after having been both partially and fully saturated. The macroscopic experimental investigation is complemented by single-fiber fragmentation tests in order to estimate the fracture properties of the fiber-matrix interface before and after aging. Furthermore, the fractographic analysis of aged specimens presented in [7] is extended with a set of observations in specimens aged at two different temperatures ($50\,^{\circ}\mathrm{C}$ and $65\,^{\circ}\mathrm{C}$) through X-ray 3D computed tomography.

For the numerical study, the multiscale and multiphysics numerical framework proposed in [18] is improved by including a new viscoelastic/viscoplastic/damage constitutive model for the resin [23] and a cohesive-zone model with friction for the fiber-matrix interfaces. Furthermore, the full-order microscopic boundary value problem embedded at each macroscopic material point is substituted by a hyper-reduced model constructed using two different model order reduction techniques [24]. The modified framework is used in an attempt to reproduce the experimentally obtained results on short-beam specimens before and after aging.

2 Mechanical tests

In this section, the effects of hygrothermal aging in a glass/epoxy material system are investigated through mechanical tests. More specifically, this work focuses on mechanical performance degradation of composite specimens subjected to interlaminar shear and of the fiber-matrix interface adhesion as measured by single-fiber fragmentation tests (SFFT). The results obtained from the micromechanical tests are used as input for the multiscale modeling framework of Section 4 while results from the macroscopic tests are used to assess model performance.

2.1 Manufacturing and conditioning

The material system used in this work is a combination of the EPIKOTE RIMR 135/EPIKURE RIMH 1366 epoxy resin reinforced with unidirectional (UD) E-Glass fiber fabrics composed of PPG Hybon 2002 fiber rovings. In order to obtain purely UD laminates, the 90° stability roving layers originally included in the commercial UD fabric were manually removed.

Dog-bone shaped single-fiber fragmentation specimens with $16\,\mathrm{mm}$ gauge length, $2\,\mathrm{mm}$ gauge width, $6.45\,\mathrm{mm}$ tab width and $2\,\mathrm{mm}$ thickness were manufactured by extracting single fibers from a fabric and positioning them in latex molds into which resin was poured and cured. For interlaminar shear strength (ILSS) tests, a 3-ply $320\,\mathrm{mm} \times 320\,\mathrm{mm} \times 2.15\,\mathrm{mm}$ panel was manufactured through vacuum infusion molding and short-beams with $21.5\,\mathrm{mm}$ length, $10.75\,\mathrm{mm}$ width and $2.15\,\mathrm{mm}$ thickness (ISO 14130 [25]) were cut from it using a CNC milling machine. The curing cycle for both specimen types consisted of $2\,\mathrm{h}$ at $30\,^{\circ}\mathrm{C}$, $5\,\mathrm{h}$ at $50\,^{\circ}\mathrm{C}$ and $10\,\mathrm{h}$ at $70\,^{\circ}\mathrm{C}$.

After manufacturing, the specimens were kept in an evacuated desiccator at $50\,^{\circ}\mathrm{C}$ and periodically weighed until a moisture-free state was reached. Sets of specimens were tested in this dry reference state. The remaining specimens were immersed in demineralized water at $50\,^{\circ}\mathrm{C}$ for different durations before being removed for testing. ILSS specimens were immersed for periods varying from $250\,\mathrm{h}$ to $2000\,\mathrm{h}$, during which water uptake measurements through weighing were periodically conducted. Single-fiber fragmentation specimens were immersed until saturation (approximately $500\,\mathrm{h}$), after which weight measurements performed on two consecutive days were used to confirm that saturation had been reached. Finally, sets of ILSS samples immersed for $500\,\mathrm{h}$ and $1000\,\mathrm{h}$ were redried in the evacuated desiccator before being tested. Weight measurements performed on two consecutive days were used to confirm that a stable dry state had been reached.

2.2 Testing

After conditioning, 10 single-fiber fragmentation specimens (5 dry, 5 saturated) were tested in an MTS test frame with $1\,\mathrm{kN}$ load cell using a custom tensile fixture suitable for small dog-bone specimens. The specimen was tested in displacement control at a rate of $0.5\,\mathrm{mm\,min^{-1}}$ until failure. A microscope camera equipped with polarized light filters was used to record the development of fiber breaks.

Sets of 10 ILSS specimens for each condition were tested in three-point bending at $1\,\mathrm{mm\,min^{-1}}$. The bending span was fixed at $11.4\,\mathrm{mm}$ and steel cylinders with diameters measuring $3.14\,\mathrm{mm}$ and $6\,\mathrm{mm}$ were used as supports and loading nose, respectively.

2.3 Results and discussion

2.3.1 Single-fiber fragmentation tests

An attempt is made at estimating the fiber-matrix interface properties through a combination of optic measurements around broken fiber fragments, the recent shear-lag model proposed by Sørensen [16] and a finite element model of the fragmentation process. Interface decohesion is modeled through a cohesive zone model with friction (Section 4.1.2) and is characterized by a decohesion strength X_{sh}, a fracture toughness G_{IIc} and a friction coefficient μ.

Fig. 1a shows a zoomed-in view of a single fiber break during a fragmentation test. Three quantities of interest are identified: The debonded length l_{d}, which delimits the region where interface adhesion is completely lost and only a constant friction stress between fiber and matrix remains, the length l_{cz} of the cohesive zone in which debonding is taking place [26], and the distance l_{p} between the brightest light spots in the fragment, which can be reliably measured even at lower magnifications and used to derive l_{d}.

For each fiber break, the debonded length l_{d} is plotted against the strain of the gauge section of the dog-bone ε, measured through videoextensometry with a $10\,\mathrm{mm}$ gauge length. A straight line is then fitted through the data points:

$$\varepsilon = \varepsilon_0 + \frac{d\,\varepsilon}{d\,(\,l_{\mathrm{d}}/r_{\mathrm{f}})}\frac{l_{\mathrm{d}}}{r_{\mathrm{f}}} \tag{1}$$

where ε_0 is an intercept parameter and r_f is the fiber radius. Care is taken to select fragments which grow with no other fragments nearby and for strain values before plastic localization occurs, two situations that violate assumptions made in the shear-lag model for data reduction [16]. Assuming a constant friction stress τ_sh along the debonded zone, the shear-lag model allows to evaluate its value from measured strain and debond length as:

$$\tau_\mathrm{sh} = \frac{1}{2}\frac{d\,\varepsilon}{d\,(\,l_\mathrm{d}/r_\mathrm{f})}E_\mathrm{f} \tag{2}$$

where E_f is the Young's modulus of the fiber. In order to compute the fracture toughness, a residual strain ε_res used to compute the strain at the fiber surface is estimated from the combined actions of curing (shrinking) and water swelling (expansion). Assuming that resin hardening takes place during the $50\,^\circ\mathrm{C}$ curing step and that chemical shrinkage due to crosslinking reactions is negligible for the present multi-step curing cycle [27], a differential strain $\varepsilon_\mathrm{res}^\mathrm{dry} = 0.0015$ is obtained. For saturated specimens, the swelling contribution is subtracted leading to $\varepsilon_\mathrm{res}^\mathrm{wet} = -0.0049$. With these values, the fracture toughness is computed as [16]:

$$G_\mathrm{IIc} = \frac{1}{4}E_\mathrm{f} r_\mathrm{f}\left(\varepsilon_0 - \varepsilon_\mathrm{res}\right)^2 \tag{3}$$

With values for τ_sh, G_IIc and the cohesive zone length l_cz, the interface strength X_sh can be estimated through a finite element model with a one-dimensional fiber with slip degrees of freedom embedded in a periodic resin slice (the reader is referred to [28] for details on the model formulation). From Fig. 1b, features with the same shapes as the ones seen through birefringence in the experiments can be observed. The cohesive strength X_sh used as input in the model has a direct influence on the resultant cohesive zone length l_cz. This means that an estimate for X_sh can be obtained by fixing the other parameters that also influence l_cz, namely the frictional stress τ_sh and the fracture energy G_IIc, and adjusting the input strength until the numerical l_cz matches the experimentally measured one. Since neither the analytical nor the numerical model take radial stresses into account, it is not possible to estimate the friction coefficient μ. For the present, the value $\mu = 0.4$, found by Naya *et al.* [1] to give the best fit with experimental data for carbon/epoxy composites, is adopted.

Measurement results are presented in Figs. 2 and 3, showing adimensionalized debonded lengths ($l_\mathrm{d}/r_\mathrm{f}$) versus fiber strain ($\varepsilon - \varepsilon_\mathrm{res}$) for 4 dry fragments and 12 wet fragments. In the plots, the different colors and point markers represent measurements on individual fragments. The reason for the lower number of dry fragments stems from the relatively low failure strain of the present epoxy resin, which caused global failure to happen in many of the tested specimens before useful debond measurements could be made. For saturated specimens, in contrast, plasticization and differential swelling promote earlier fragment development.

The averages and standard deviations of the obtained properties are shown in Table 1, computed with $l_\mathrm{cz} = 0.15\,\mathrm{mm}$, considered constant throughout the test. Due to the indirect nature of the estimation procedure, a lack of literature consensus on the definition of a debonded region with constant shear stress [16, 26], uncertainties related to the amount of thermal and chemical residual strains and the large scatter observed between fragments, these values only provide a rough estimate of interface performance. Further experiments and model development are therefore necessary. Nevertheless, results indicate loss of friction and degraded adhesion properties after aging, on average.

2.3.2 Interlaminar shear tests

For the macromechanical part of this study, hygrothermal degradation is measured in unidirectional short beams tested in three-point bending. A measure of the transverse shear stress at the

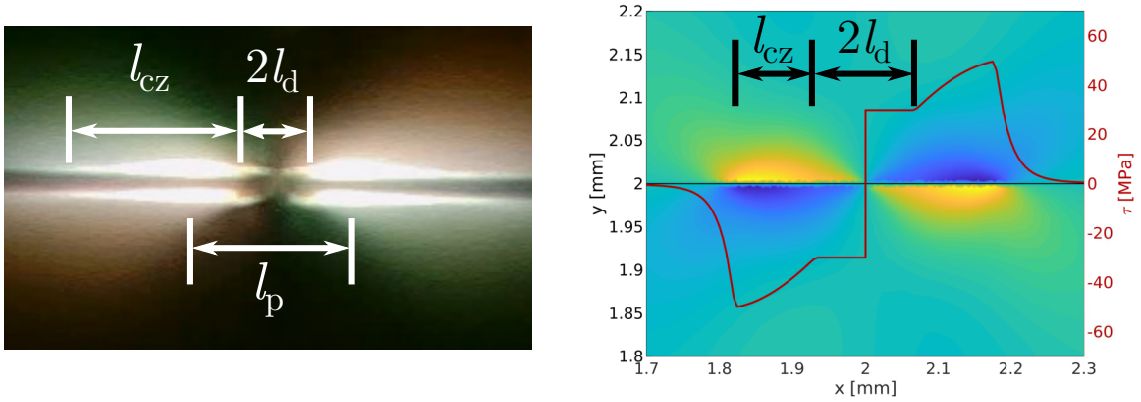

(a) Experiment (b) Simulation

Figure 1: A fiber break as observed during an experiment and through numerical simulation, showing the quantities of interest for property estimation.

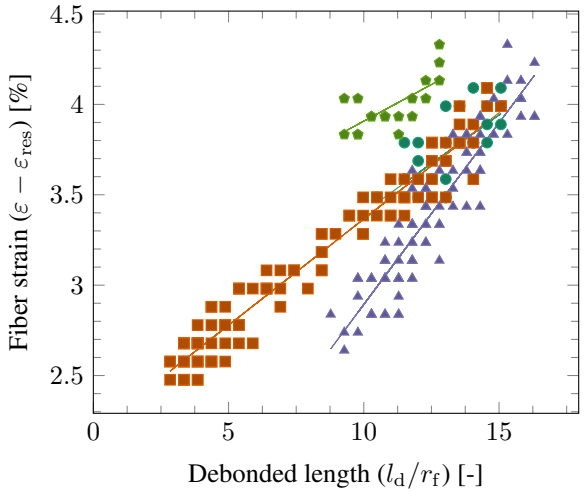

Figure 2: SFFT results for dry specimens.

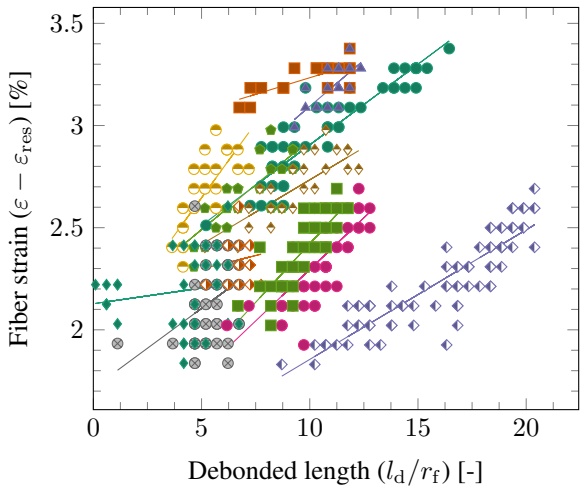

Figure 3: SFFT results for saturated specimens.

	Dry	Saturated
τ_{sh} [MPa]	46.27 ± 16.37	27.31 ± 13.22
G_{IIc} [N/mm]	0.093 ± 0.056	0.067 ± 0.031
X_{sh} [MPa]	52.0	30.0

Table 1: Interface properties estimated through single-fiber fragmentation tests.

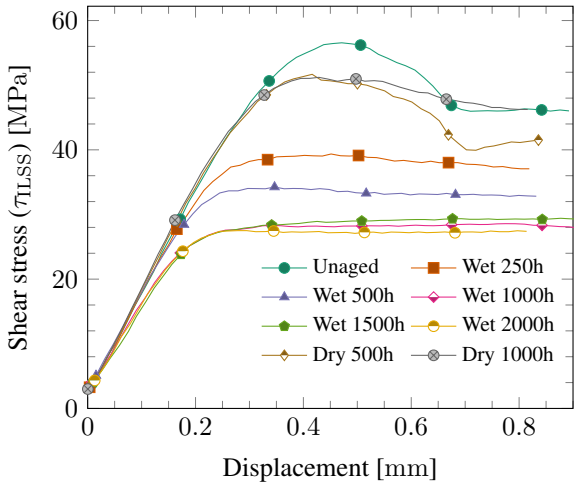

Figure 4: Interlaminar shear strength (ILSS) results.

center of the short-beam specimens is obtained from the force signal F of the test frame [25]:

$$\tau_{\mathrm{ILSS}} = \frac{3}{4}\frac{F}{bh} \tag{4}$$

where b and h are the specimen width and thickness, respectively, measured after conditioning. Fig. 4 plots the thus computed shear stress versus crosshead displacement for different aging times. To avoid clutter, only one representative specimen for each condition is shown. Average values of the maximum attained stress (interlaminar shear strength) for each condition are presented in Table 2.

In order to relate changes in strength to the water concentration in the specimens, the water uptake is computed as:

$$w_{\%}(t) = 100\frac{m(t) - m_{\mathrm{dry}}}{m_{\mathrm{dry}}} \tag{5}$$

where $m(t)$ is the specimen mass at time t and m_{dry} is a reference mass measured before aging. Water uptake and average interlaminar shear strength values (wet and redried) are plotted against time in Fig. 5. It is important to note that unsaturated samples have a non-uniform water concentration field. The associated $w_{\%}$ values for these samples are therefore the volume averages of the concentration and do not represent the exact amount of water at material regions where interlaminar failure occurs.

The results point to a gradual strength decrease as the specimens absorb water, with up to $50\,\%$ degradation after $1000\,\mathrm{h}$, a point in time when the diffusion process subsides and the specimen is saturated with water. A clear correlation can therefore be identified between the amount of water in the specimen and its interlaminar shear performance.

After reaching a stable value at saturation, the strength and uptake remain approximately constant between $1000\,\mathrm{h}$ and $2000\,\mathrm{h}$, suggesting that long-term chemical degradation of the interface

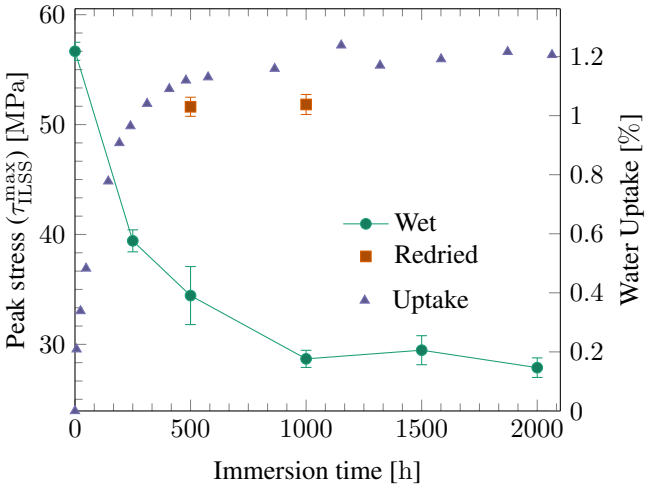

Figure 5: ILSS peak stresses for wet and redried specimens and water uptake for different immersion times.

[7] is negligible for the short aging durations considered in this work. Nevertheless, a small part of the degradation is irreversible, as evidenced by the redried tests performed after $500\,\mathrm{h}$ and $1000\,\mathrm{h}$ of immersion. The numerical models of Section 4 will help elucidate if this permanent degradation arises from swelling-induced microscopic failure events or if it is instead caused by a fast chemical degradation process taking place at the same time scale as that of the diffusion phenomenon.

	Unaged	250h	500h	1000h	1500h	2000h
Tested wet						
$\tau_{\mathrm{ILS}}^{\mathrm{max}}$ [MPa]	-	39.4 ± 1.0	34.4 ± 2.6	28.7 ± 0.9	29.5 ± 1.3	27.9 ± 0.9
Tested dry						
$\tau_{\mathrm{ILS}}^{\mathrm{max}}$ [MPa]	56.7 ± 0.8	-	51.6 ± 0.9	51.8 ± 0.9	-	-

Table 2: ILSS values for short-beam specimens.

3 X-Ray computed tomography

Results from mechanical tests point to the occurrence of material damage after hygrothermal aging. It is therefore interesting to employ microscopic observation techniques in an attempt to observe degradation events in specimens after aging but before being mechanically tested.

3.1 Conditioning

For this part of the study, one additional short-beam specimen was conditioned at $50\,^{\circ}\mathrm{C}$ for the longer period of $5000\,\mathrm{h}$ in order to investigate both short- and long-term hygrothermal degradation. Furthermore, a specimen was conditioned at $65\,^{\circ}\mathrm{C}$ for $500\,\mathrm{h}$ so that degradation at two different temperatures can be compared. Observations on an unaged specimen are also performed for comparison.

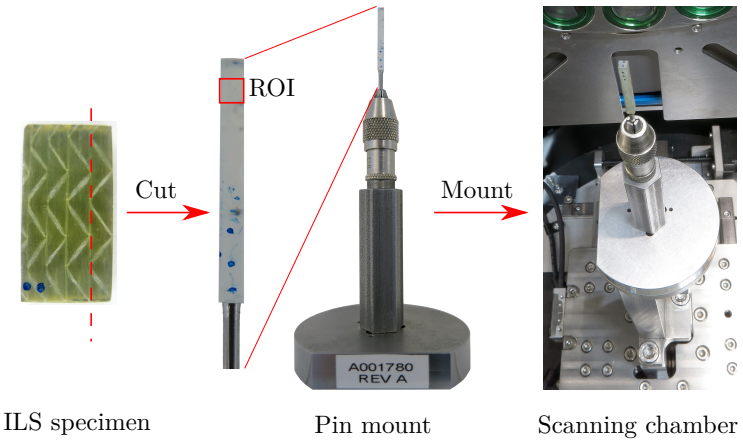

Figure 6: Specimen preparation and scanning procedure, showing the Region of Interest (ROI) for the scans.

Parameter	LFoV	SFoV
Magnification [-]	4.0x	20.0x
Beam voltage [keV]	30	45
Beam power [W]	2	3.5
Exposure time [s]	13-18	40
No. of projections [-]	5201-5801	3801
Field of view [μm]	2500	500
Scanning time [h/scan]	32	45

Table 3: Scanning parameters for small and large field of view scans.

3.2 Scanning

Three-dimensional X-ray computed tomography scans of the specimens are performed using a Zeiss Xradia Versa 520 scanner. Strip specimens with nominal dimensions $2.15\,\mathrm{mm} \times 2.15\,\mathrm{mm} \times 21.5\,\mathrm{mm}$ are cut from the short-beams and glued to an aluminum pin which is then attached to a special mount and positioned in the scanning chamber between an X-ray source and a detector (Fig. 6). A motorized x-y-z stage is used to align the scanning Region of Interest (ROI) with the source and suitable source-sample and sample-detector distances are chosen in order to obtain the desired scanning Field of View (FoV). During the scans, tomographic projections of the ROI are taken as the sample holder is gradually rotated. As a post-processing step, the projections are combined to form three-dimensional reconstructions of the scanned volumes[1].

As scanning resolution is inversely proportional to the size of the scanned volume but the study involves searching for relatively small features (*e.g.* interfacial debonding cracks on single fibers), a sequential scanning strategy is adopted. First, a large field of view (*LFoV*) scan is performed and regions of interest close to the center and surface of the specimens are chosen for small field of view scans (*SFoV*). Parameters for both scan types are shown in Table 3.

[1]For the complete scan data, the reader is referred to [29]. The reader is also encouraged to scan the QR codes embedded in the figures for videos of the reconstructed volumes.

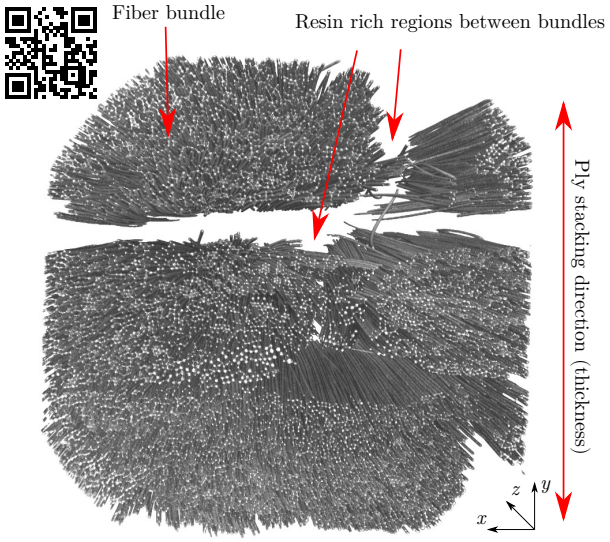

Figure 7: Reconstructed scanned volume of a dry specimen (LFoV).

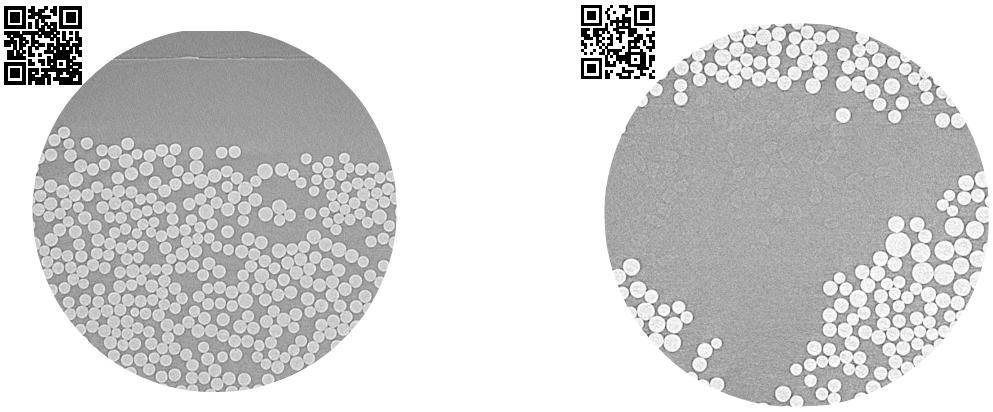

(a) Specimen surface

(b) Specimen center

Figure 8: Small field of view scans of a reference specimen.

3.3 Results and discussion

Fig. 7 shows the reconstructed cylindrical volume resulting from the LFoV scan of an unaged specimen. The locations of the fiber bundles and resin rich regions along the three plies that make up the specimen can be clearly identified. Fig. 8 shows SFoV scans of the same specimen. No visible failure can be identified for this condition.

More interesting features are observed on the specimen aged at $65\,^{\circ}\mathrm{C}$. The LFoV scan of Fig. 9 shows a region of extensive interface debonding close to the specimen surface. By moving along the specimen length (z-axis), it is possible to observe the crack and its associated fracture process zone. Similar failure loci can also be observed at multiple other points close to the specimen surface. The SFoV scan of Fig. 10a shows one of these locations, with interface debonding both in isolated fibers and propagating among groups of fibers. In contrast, a zoomed-in scan close to the center of the specimen reveals only barely visible debonding cracks (Fig. 10b).

For the specimen aged at $50\,^{\circ}\mathrm{C}$, only minor failure events can be observed (Fig. 11). Material degradation is therefore markedly worse for specimens aged at $65\,^{\circ}\mathrm{C}$. Furthermore, the new spaces formed by crack opening promote additional water uptake, with a moisture content of $1.5\,\%$

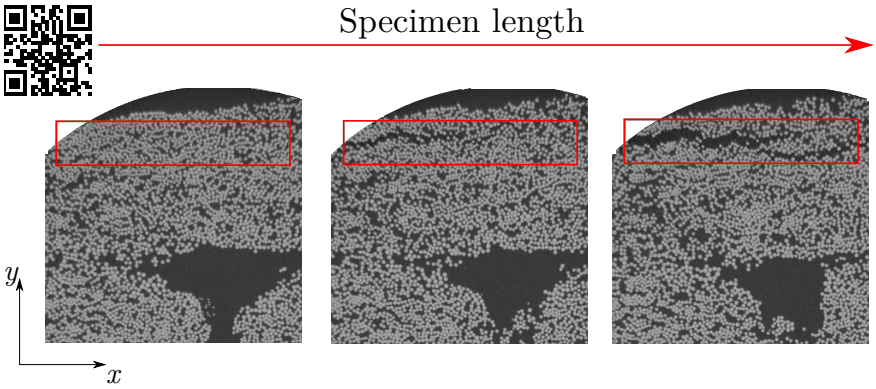

Figure 9: Large field of view scan of a specimen aged at 65 °C showing a large debonding crack.

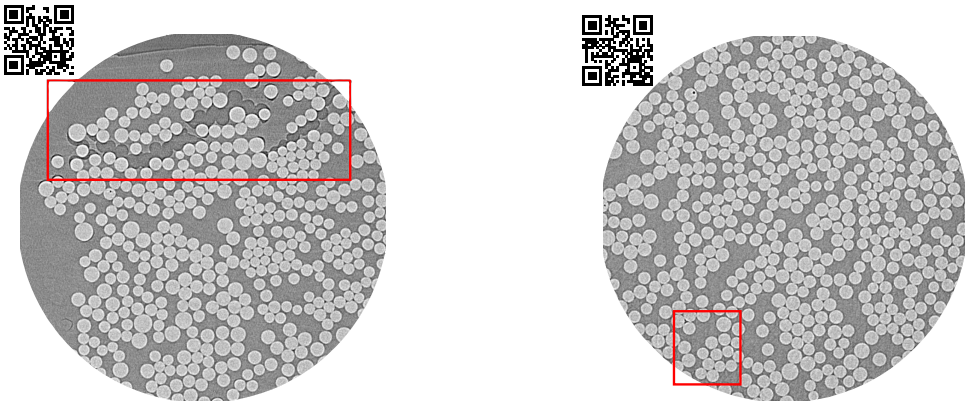

(a) Specimen surface

(b) Specimen center

Figure 10: Small field of view scans of a specimen aged at 65 °C, with cracks marked in red.

measured after 500 h of immersion at 65 °C, higher than the observed saturation level of 1.2 % for 50 °C specimens (Fig. 5). Similar behavior has been observed in other studies [7, 30, 4, 9].

Based on their proximity to the surface and on the large openings between crack faces, it can be hypothesized that such debonding cracks, initiated through differential swelling, propagate aided by an osmotic process that leads to accelerated water uptake and hydrostatic pressure between crack faces. This is similar to the behavior reported for glass/polyester composites by Gautier *et al.* [4] and would imply that hydrolytic chemical reactions take place involving either the interface sizing or the glass fibers, creating leachates that drive the ensuing osmosis.

Activation of such osmotic mechanism would therefore depend on the differences in speed between diffusion, chemical reaction and leaching. For specimens aged at 50 °C, it is reasonable to suppose that diffusion and reaction are slow enough to allow for reaction products to be leached before significant osmosis takes place. Nevertheless, hydrolytic reactions would permanently degrade interface performance, which corresponds with the measured strength loss in the redried specimens of Section 2.3.2, and cause loss of material through leaching, as reported by the authors in [7].

4 Numerical modeling

The aging process followed by mechanical testing is numerically simulated using the Finite Element Method in order to reproduce the experimentally observed material degradation. Since ag-

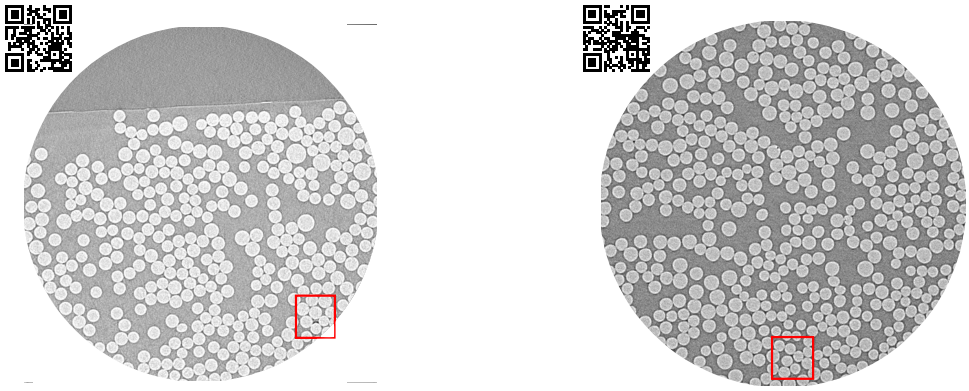

(a) Specimen surface

(b) Specimen center

Figure 11: Small field of view scans of a specimen aged at 50 °C, with small debonding cracks marked in red.

ing affects each material constituent differently, a micromechanical modeling strategy is adopted. In order to realistically simulate tests on specimens with non-homogeneous water concentration fields, a multiscale approach is used to model both micro and macroscales concurrently. In this section, the resultant numerical framework is briefly presented in order to keep the study self-contained. For more detailed formulations, the interested reader will be referred to additional literature on the subject.

4.1 Microscopic material models

4.1.1 Viscoelastic-Viscoplastic-Damage epoxy

An epoxy model with viscoelastic, viscoplastic and damage components is adopted in order to take into account rate-dependent plasticity and damage activation. The present development highlights the main ingredients of a model recently proposed by the authors [23] with a slightly modified damage model inspired by the work of Arefi *et al.* [31].

The model is based on an additive strain decomposition in elastic, plastic, thermal and swelling parts:

$$\boldsymbol{\varepsilon} = \boldsymbol{\varepsilon}^{\mathrm{e}} + \boldsymbol{\varepsilon}^{\mathrm{p}} + \boldsymbol{\varepsilon}^{\mathrm{th}} + \boldsymbol{\varepsilon}^{\mathrm{sw}} \tag{6}$$

where the thermal and swelling contributions are given by:

$$\boldsymbol{\varepsilon}^{\mathrm{th}} = \alpha_{\mathrm{t}} \left(T - T_0\right) \mathbf{I} \quad \boldsymbol{\varepsilon}^{\mathrm{sw}} = \alpha_{\mathrm{sw}} c \mathbf{I} \tag{7}$$

with α_{t} and α_{sw} being the thermal and swelling expansion coefficients, respectively, $\mathbf{I}$ being the identity matrix, c being the water concentration and T and T_0 the actual temperature and the temperature at which resin hardening took place, respectively.

The elastic strains are used to compute the stresses by integrating the complete strain time history through the use of a time variable $\tilde{t}$:

$$\widetilde{\boldsymbol{\sigma}}(t) = \mathbf{D}^{\infty} \boldsymbol{\varepsilon}^{\mathrm{e}}(t) + \int_0^t \mathbf{D}^{\mathrm{ve}}(t - \tilde{t}) \frac{\partial \boldsymbol{\varepsilon}^{\mathrm{e}}(\tilde{t})}{\partial \tilde{t}} d\tilde{t} \tag{8}$$

The stresses are composed of an inviscid contribution related to the long-term stiffness $\mathbf{D}^{\infty}$ and a viscous contribution driven by the time-dependent viscoelastic stiffness $\mathbf{D}^{\mathrm{ve}}$. This viscous contribution is represented by a Prony series of bulk and shear stiffness elements arranged in parallel, with stiffnesses K_u and G_v and relaxation times k_u and g_v, respectively.

Plastic strain develops when a pressure-dependent paraboloidal yield surface is reached:

$$f_{\mathrm{p}}(\boldsymbol{\sigma}, \varepsilon_{\mathrm{eq}}^{\mathrm{p}}) = 6J_2 + 2I_1\left(\sigma_c(\varepsilon_{\mathrm{eq}}^{\mathrm{p}}) - \sigma_t(\varepsilon_{\mathrm{eq}}^{\mathrm{p}})\right) - 2\sigma_c(\varepsilon_{\mathrm{eq}}^{\mathrm{p}})\sigma_t(\varepsilon_{\mathrm{eq}}^{\mathrm{p}}) \tag{9}$$

where J_2 and I_1 are the second invariant of the deviatoric stress tensor and the first invariant of the stress tensor, respectively, and σ_{c} and σ_{t} are the yield stresses in compression and tension, respectively. Hardening is taken into account through the dependency of the yield stresses on the equivalent plastic strain $\varepsilon_{\mathrm{eq}}^{\mathrm{p}}$. The non-associative plastic flow $\Delta\boldsymbol{\varepsilon}^{\mathrm{p}}$ is dictated by the plastic multiplier γ which in turn evolves in a viscous manner:

$$\Delta\boldsymbol{\varepsilon}^{\mathrm{p}} = \Delta\gamma\left(3\mathbf{S} + \frac{2}{9}\alpha I_1\mathbf{I}\right) \quad \Delta\gamma = \begin{cases} \frac{\Delta t}{\eta_{\mathrm{p}}}\left(\frac{f_{\mathrm{p}}}{\sigma_{\mathrm{t}}^0\sigma_{\mathrm{c}}^0}\right)^{m_{\mathrm{p}}}, & \text{if } f_{\mathrm{p}} > 0 \\ 0, & \text{if } f_{\mathrm{p}} \leq 0 \end{cases} \tag{10}$$

where $\mathbf{S}$ is the deviatoric stress tensor, α is a factor related to the plastic Poisson's ratio ν_{p}, η_{p} and m_{p} are the viscoplastic modulus and exponent, respectively, σ_{t}^0 and σ_{c}^0 are the initial yield stresses, and Δt is a time step.

A continuum damage model is adopted in order to model resin fracture. A damage variable d_{m} is adopted and the damaged stresses are computed as:

$$\boldsymbol{\sigma} = \mathbf{D}^{\mathrm{s}}\mathbf{H}_0\widetilde{\boldsymbol{\sigma}} \tag{11}$$

where $\widetilde{\boldsymbol{\sigma}}$ and $\mathbf{H}_0$ are the stresses and compliance matrix computed for the pristine material (*i.e.* with $d_{\mathrm{m}} = 0$) and $\mathbf{D}^{\mathrm{s}}$ is a secant stiffness matrix written as:

$$\mathbf{D}^{\mathrm{s}} = \begin{bmatrix} \kappa & \beta & \beta & 0 & 0 & 0 \\ \beta & \kappa & \beta & 0 & 0 & 0 \\ \beta & \beta & \kappa & 0 & 0 & 0 \\ 0 & 0 & 0 & \widehat{G}(1-d_{\mathrm{m}}) & 0 & 0 \\ 0 & 0 & 0 & 0 & \widehat{G}(1-d_{\mathrm{m}}) & 0 \\ 0 & 0 & 0 & 0 & 0 & \widehat{G}(1-d_{\mathrm{m}}) \end{bmatrix} \tag{12}$$

and the factors κ and β are given by:

$$\kappa = \frac{\widehat{E}(1-d_{\mathrm{m}})(1-\widehat{\nu}(1-d_{\mathrm{m}}))}{(1+\widehat{\nu}(1-d_{\mathrm{m}}))(1-2\widehat{\nu}(1-d_{\mathrm{m}}))} \quad \beta = \frac{\widehat{E}\widehat{\nu}(1-d_{\mathrm{m}})^2}{(1+\widehat{\nu}(1-d_{\mathrm{m}}))(1-2\widehat{\nu}(1-d_{\mathrm{m}}))} \tag{13}$$

with $\widehat{G}$ being the viscoelastic shear modulus and $\widehat{E}$ and $\widehat{\nu}$ the viscoelastic Young's modulus and Poisson's ratio, computed as:

$$\widehat{E} = 2\widehat{G}\,(1+\widehat{\nu}) \quad \widehat{\nu} = \frac{3\widehat{K} - 2\widehat{G}}{2\widehat{G} + 6\widehat{K}} \tag{14}$$

This definition of the secant stiffness deviates from the original model proposed by the authors [23] by also applying a degradation to $\widehat{\nu}$. This makes the model more suitable for use in dense finite element meshes by avoiding spurious hardening on damaged elements constrained by bands of elements undergoing elastic unloading.

A pressure-dependent paraboloidal fracture surface is adopted:

$$f_{\mathrm{d}}(\widetilde{\boldsymbol{\sigma}}, r) = \frac{3\widetilde{J}_2}{X_{\mathrm{c}}X_{\mathrm{t}}} + \frac{\widetilde{I}_1(X_{\mathrm{c}} - X_{\mathrm{t}})}{X_{\mathrm{c}}X_{\mathrm{t}}} - r \quad \Rightarrow \quad f_{\mathrm{d}}(\widetilde{\boldsymbol{\sigma}}, r) = \Lambda - r \tag{15}$$

where r is an internal variable which controls damage evolution and $X_{\mathrm{c}} = X_{\mathrm{c}}(\Upsilon)$ and $X_{\mathrm{t}} = X_{\mathrm{t}}(\Upsilon)$ are the fracture strengths in compression and tension, respectively, which are functions of

the cumulative dissipated energy $\Upsilon = \Upsilon_{\mathrm{ve}} + \Upsilon_{\mathrm{vp}}$ [23]. Through a shrink in the fracture surfaces as energy dissipates, rate-dependent damage activation is taken into account.

At each time step, the variable r is explicitly updated as:

$$r_{t_{n+1}} = \max\left\{1, \max_{0\leq t\leq t_{n+1}} \Lambda_t\right\} \tag{16}$$

and the damage variable is computed based on the linear softening law proposed by Arefi *et al.* [31]:

$$d_{\mathrm{m}} = \begin{cases} \dfrac{\varepsilon_{\mathrm{f}}(\varepsilon_{\mathrm{eq}} - \varepsilon_0)}{\varepsilon_{\mathrm{eq}}(\varepsilon_{\mathrm{f}} - \varepsilon_0)}, & \varepsilon_{\mathrm{eq}} \leq \varepsilon_{\mathrm{f}} \\ 1, & \varepsilon_{\mathrm{eq}} > \varepsilon_{\mathrm{f}} \end{cases} \tag{17}$$

where the strains at the beginning (ε_0) and end (ε_{f}) of the softening regime are determined based on an uniaxial tensile test:

$$\varepsilon_0 = X_{\mathrm{t}} \quad \varepsilon_{\mathrm{f}} = \frac{2G_{\mathrm{c}}\widehat{E}}{l_{\mathrm{e}}X_{\mathrm{t}}} \tag{18}$$

with G_{c} being the resin fracture toughness and l_{e} the characteristic finite element length [32]. Finally, $\varepsilon_{\mathrm{eq}}$ is a scalar measure of the strain state:

$$\varepsilon_{\mathrm{eq}} = \frac{-q + \sqrt{q^2 - 4pu}}{2p} \tag{19}$$

and the parameters q, p and u are given by:

$$\begin{gathered} q = 2a(1-a)b\varepsilon_{\mathrm{f}} + (1+2a)c \quad u = b(a\varepsilon_{\mathrm{f}})^2 - 2ac\varepsilon_{\mathrm{f}} - rX_{\mathrm{t}}X_{\mathrm{c}} \\ p = b(1-a)^2 \quad a = \frac{\widehat{\nu}X_{\mathrm{t}}}{\widehat{E}(\varepsilon_{\mathrm{f}} - \varepsilon_0)} \\ b = \left(\frac{\widehat{E}}{1+\widehat{\nu}}\right)^2 \quad c = \left(\frac{\widehat{E}}{1-2\widehat{\nu}}\right)(X_{\mathrm{c}} - X_{\mathrm{t}}) \end{gathered} \tag{20}$$

4.1.2 Cohesive interfaces with friction

Fiber-matrix interface debonding is modeled using interface elements with softening behavior dictated by a cohesive-zone model. The model used in this work is based on the one presented in [18] but is modified to include a friction component, following the formulation by Alfano and Sacco [33]. The displacement jump is additively split into elastic and friction contributions:

$$[\![\mathbf{u}]\!] = [\![\mathbf{u}]\!]^{\mathrm{e}} + [\![\mathbf{u}]\!]^{\mu} \tag{21}$$

and a friction traction contribution $\mathbf{t}^{\mu}$ is added to the original cohesive traction:

$$\mathbf{t} = (1 - d_{\mathrm{i}})\, K[\![\mathbf{u}]\!] + d_{\mathrm{i}}\mathbf{t}^{\mu} \tag{22}$$

where K is an initial stiffness, $\mathbf{t}^{\mu} = K\left([\![\mathbf{u}]\!] - [\![\mathbf{u}]\!]^{\mu}\right)$, and d_{i} is a damage variable which represents the degree of interface debonding.

The evolution of d_{i} with the total displacement jump $[\![\mathbf{u}]\!]$ remains unchanged from the original model [18] and will be omitted for compactness. Friction evolves in a way analogous to non-associative plasticity. The displacement jump $[\![\mathbf{u}]\!]^{\mu}$ is updated when a Coulomb friction surface is reached:

$$f_{\mu}(\mathbf{t}^{\mu}) = \mu\langle t^{\mu}_{\mathrm{n}}\rangle_{-} + t^{\mu}_{\mathrm{sh}} \tag{23}$$

where the $\langle\cdot\rangle_-$ operator returns the negative part of its operand and $t^\mu_{\rm sh} = \sqrt{(t^\mu_{\rm s})^2 + (t^\mu_{\rm t})^2}$ is the normalized shear traction. Finally, the friction flow rule is given by:

$$\Delta[\![\mathbf{u}]\!]^\mu = \Delta\lambda \begin{bmatrix} 0 \\ t^\mu_{\rm sh} \\ \hline |t^\mu_{\rm sh}| \end{bmatrix} \quad \Delta\lambda = \frac{f_\mu}{K} \tag{24}$$

which is complemented by the Kuhn-Tucker conditions $\dot\lambda \geq 0$, $f_\mu \leq 0$, $\dot\lambda f_\mu = 0$.

4.1.3 Hygrothermal aging

Plasticization and fiber-matrix interface weakening are modeled with an additional degradation variable $d_{\rm w}$ which is a function of the water concentration c of the material point:

$$d_{\rm w} = \frac{d^\infty_{\rm w}}{c_\infty} c \tag{25}$$

where c_∞ and $d^\infty_{\rm w}$ are the water concentration and material degradation at saturation, respectively. Since only tests at dry and saturated states are available for resin [23] and interface (Section 2.3.1), a linear evolution of $d_{\rm w}$ is adopted. The degradation variable is then used to modify the resin properties as follows:

$$\widehat{E}_{\rm w} = (1 - d_{\rm w})\widehat{E} \tag{26}$$

$$\sigma^{\rm w}_{\rm c} = (1 - d_{\rm w})\sigma_{\rm c}, \;\; \sigma^{\rm w}_{\rm t} = (1 - d_{\rm w})\sigma_{\rm t} \tag{27}$$

$$X^{\rm w}_{\rm c} = (1 - d_{\rm w})X_{\rm c}, \;\; X^{\rm w}_{\rm t} = (1 - d_{\rm w})X_{\rm t}, \;\; G^{\rm w}_{\rm c} = (1 - d_{\rm w})^2 G_{\rm c} \tag{28}$$

where the squared toughness degradation is adopted for the sake of numerical stability, since no reliable measurements of saturated fracture toughness on the present resin system are available and only an estimation of its value based on tensile tests is adopted [23].

For the fiber-matrix interface, a similar degradation approach is adopted, but the change in fracture toughness is modified in order to reflect the results obtained on the fragmentation tests of Section 2.3.1:

$$X^{\rm w}_{\rm n} = (1 - d_{\rm w})X_{\rm n} \quad X^{\rm w}_{\rm sh} = (1 - d_{\rm w})X_{\rm sh} \quad G^{\rm w}_{\rm Ic} = \sqrt{1 - d_{\rm w}}G_{\rm Ic} \quad G^{\rm w}_{\rm IIc} = \sqrt{1 - d_{\rm w}}G_{\rm IIc} \tag{29}$$

where $X_{\rm n}$, $G_{\rm Ic}$, $X_{\rm sh}$ and $G_{\rm IIc}$ are the interface strength and fracture toughness in mode I and modes II and III, respectively. Since only mode II properties are available for the present material system (Table 1), they are also used to describe decohesion in mode I in the present study.

Previous experiments on neat resin [7] point to complete stiffness and strength recovery after a single immersion-redrying cycle at $50\,^\circ\mathrm{C}$. Hygrothermal degradation of the resin is therefore modeled as a reversible process. Due to the lack of experimental data on redried fragmentation specimens, interface degradation is also modeled as reversible.

4.2 Multiscale/multiphysics framework

The microscopic material models of Section 4.1 are used in conjunction with a multiscale/multiphysics framework in order to predict the behavior of macroscopic material specimens subjected to aging followed by mechanical loads. The framework is presented in detail in [18] and will be briefly summarized in the following.

4.2.1 Diffusion model

A Fickian diffusion model is used to predict the evolution of the macroscopic water concentration field with aging time. The changes in concentration and the resultant mass flux $\mathbf{j}$ are computed by:

$$\dot{c}^{\Omega} + \frac{\partial}{\partial \mathbf{x}^{\Omega}} \cdot \mathbf{j}^{\Omega} = 0 \quad \mathbf{j}^{\Omega} = -\mathbf{D}^{\Omega} \frac{\partial c}{\partial \mathbf{x}^{\Omega}} \tag{30}$$

where $\mathbf{D}$ is an orthotropic diffusivity matrix and the superscript Ω indicates macroscopic quantities. The water concentration at each material point is downscaled to an embedded micromodel (FE^2) and is considered constant inside the microdomain. This solution implicitly assumes that water diffusion in the resin is well represented by a one-phase Fick solution. The diffusivity vector is pre-computed through a homogenization process [34] and is considered constant, leading to a linear transient diffusion problem.

4.2.2 Stress model

The nonlinear stress problem is solved iteratively using a Newton-Raphson solver and takes place after the water concentration field is updated (staggered coupling). An equilibrium problem is solved at both scales:

$$\frac{\partial}{\partial \mathbf{x}^{\Omega}} \cdot \boldsymbol{\sigma}^{\Omega} = \mathbf{0} \quad \frac{\partial}{\partial \mathbf{x}^{\omega}} \cdot \boldsymbol{\sigma}^{\omega} = \mathbf{0} \tag{31}$$

where the superscript ω indicates microscopic quantities. No assumptions are made regarding the constitutive behavior of the macroscopic material. Instead, stresses and stiffnesses are obtained through homogenization of the microscopic response: Strains are applied as prescribed displacements at the corners of the embedded micromodels, the micro boundary value problems are solved and volume averages of stiffnesses and stresses are upscaled.

4.3 Reduced-order modeling

The multiscale/multiphysics framework of Section 4.2 involves solving a microscopic boundary value problem for each macroscopic integration point on every iteration of every time step. In turn, solving each micromodel involves solving a nonlinear finite element equilibrium problem featuring dense meshes and complex material models. The resultant computational effort is, therefore, exceedingly high. In this section, two model order reduction techniques will be briefly presented which allow for efficiently solving the microscopic equilibrium problems with minimum loss of accuracy. For more detailed formulations and an assessment of their efficacy, the reader is referred to [24].

4.3.1 Proper Orthogonal Decomposition (POD)

Instead of solving for the full micro displacement field $\mathbf{u}^{\omega}$ with N unknowns, one can instead choose a number $n \ll N$ of displacement modes arranged in a matrix $\boldsymbol{\Phi} \in \mathbb{R}^{N \times n}$ and solve for their relative contributions $\boldsymbol{\alpha}$, which reduces the size of the equilibrium system to n unknowns. The original displacement field is the linear combination of the n modes:

$$\mathbf{u} = \boldsymbol{\Phi}\boldsymbol{\alpha} \tag{32}$$

which leads to reduced versions of the global internal force and tangent stiffness:

$$\mathbf{f}_{\mathrm{r}}^{\omega} = \boldsymbol{\Phi}^{\mathrm{T}}\mathbf{f}^{\omega} \quad \mathbf{K}_{\mathrm{r}}^{\omega} = \boldsymbol{\Phi}^{\mathrm{T}}\mathbf{K}^{\omega}\boldsymbol{\Phi} \tag{33}$$

where a subscript r denotes a reduced entity. The displacement modes are computed before the multiscale analysis by subjecting the micromodel to representative loading situations and applying

a truncated Singular Value Decomposition (SVD) process to the obtained displacement snapshots [24, 35].

4.3.2 Empirical Cubature Method (ECM)

Although POD reduces the size of the global equilibrium equation, computing $\mathbf{f}^{\omega}$ and $\mathbf{K}^{\omega}$ still involves computing complex constitutive models for all M integration points of the microscopic domain ω. Further acceleration (so-called *hyper-reduction*) can be achieved by choosing a number $m \ll M$ of integration points and computing modified integration weights $\boldsymbol{\varpi}$ in order to obtain a good approximation of the reduced global internal force vector with only a small fraction of the effort:

$$\mathbf{f}^{\omega} = \int_{\omega} \mathbf{f}\, d\omega \approx \sum_{i=1}^{m} \mathbf{f}\left(\mathbf{x}_i^{\omega}\right) \varpi_i \tag{34}$$

The reduced set of points and weights is chosen by minimizing the error between the original and approximated versions of $\mathbf{f}_{\mathrm{r}}^{\omega}$ using a least-squares point selection algorithm [24, 21].

4.4 Results and discussion

The preceding numerical framework was implemented in an in-house Finite Element code built using the open-source *Jem/Jive* C++ library [36]. The analyses are executed on a workstation equipped with an Intel Xeon E5-2650 processor and $64\,\mathrm{Gb}$ of RAM. Evaluation of the micromodels during concurrent multiscale analyses is performed in parallel. The microscopic domain is represented by a periodic microcell with 16 fibers. Based on a previously performed RVE study [18], this microdomain size is considered to represent the macroscopic behavior of the unidirectional composite material with reasonable accuracy. The micromodel is discretized with 3198 wedge finite elements and 337 interface elements around the fibers. The fibers are modeled as linear-elastic, while the material models of Section 4.1 are used for the resin and interfaces. The adopted microscopic material properties are shown in Table 4.

In order to employ the micromodel in a macroscopic simulation of an ILSS test, a reduced-order model is first trained to accurately represent the elastic, plastic and fracture response of a micromodel subjected to a combination of interlaminar shear, hygrothermal aging and residual stresses. The load cases used in the training process are shown in Fig. 12. A strain rate $\dot{\varepsilon} = 5 \times 10^{-2}\,\mathrm{s}^{-1}$ is adopted for all cases with mechanical loads. For cases including water concentration, it is applied in steps from an initially dry state to a concentration value of $3.2\,\%$, corresponding to the saturation level of the epoxy resin. For residual stresses, a temperature variation $\Delta T = -27\,^{\circ}\mathrm{C}$ is applied in steps. For cases combining environmental loads with mechanical strains, water is applied first, followed by temperature and finally by prescribed displacements. Each elastic case is run for three steps in order to provide the reduced model with information on the decay of viscoelastic stresses. The inelastic cases are run until a stress drop is observed, indicating strain localization. Since failure occurs due to transverse shear, it manifests as a single horizontal localization band which runs between the left and right boundaries of the RVE.

The original model is reduced from $N = 12\,138$ to $n = 21$ degrees of freedom in a first reduction stage (POD). This reduced model is then subjected to a second training stage in order to select a reduced set of integration points, with a reduction from $M = 4546$ to $m = 589$ integration points. Fig. 13 shows the homogenized stress-strain responses for both the dry and saturated conditions of the full micromodel and its POD-reduced counterpart (after the first reduction phase). The reduced model is able to accurately represent the full response of the cases used for training, although the prediction of the softening response of the saturated material is relatively less accurate due to the sharp softening branch caused by the influence of displacement modes obtained from

Glass fibers				
K_∞ [MPa]	43452			
G_∞ [MPa]	29918			
α_t [K^{-1}]	$5.4 \cdot 10^{-6}$			
Epoxy resin				
K_∞ [MPa]	3205			
G_∞ [MPa]	912			
K_u [MPa]	125	182	625	143
G_v [MPa]	36	52	178	41
k_u [s]	$4.16 \cdot 10^{-2}$	$2.30 \cdot 10^{0}$	$4.22 \cdot 10^{1}$	$3.11 \cdot 10^{4}$
g_v [s]	$1.46 \cdot 10^{-1}$	$8.08 \cdot 10^{0}$	$1.48 \cdot 10^{2}$	$1.09 \cdot 10^{5}$
σ_t [MPa]	$64.80 - 33.6\mathrm{e}^{-\epsilon^\mathrm{p}_\mathrm{eq}/0.003407} - 10.21\mathrm{e}^{-\epsilon^\mathrm{p}_\mathrm{eq}/0.06493}$			
σ_c [MPa]	$81.0 - 42.0\mathrm{e}^{-\epsilon^\mathrm{p}_\mathrm{eq}/0.003407} - 12.77\mathrm{e}^{-\epsilon^\mathrm{p}_\mathrm{eq}/0.06493}$			
η_p [s]	$3.49 \cdot 10^{12}$			
m_p [-]	7.305			
ν_p [-]	0.32			
X_t [MPa]	$83.8 - 5.99\,\Upsilon$			
X_c [MPa]	$104.7 - 7.48\,\Upsilon$			
G_c [N/mm]	1.9			
d_w^∞ [-]	0.14			
α_t [K^{-1}]	$6.0 \cdot 10^{-5}$			
α_sw [$\%^{-1}$]	0.002			
Fiber-matrix interface				
K [MPa]	10^6			
$X_\mathrm{n}/X_\mathrm{sh}$ [MPa]	52			
$G_\mathrm{Ic}/G_\mathrm{IIc}$ [N/mm]	0.093			
μ [-]	0.4			
d_w^∞ [-]	0.42			
Diffusion				
c_∞ [%]	3.2			
D_x/D_y [µm/s]	0.520			
D_z [µm/s]	1.638			

Table 4: Properties used for numerical modeling.

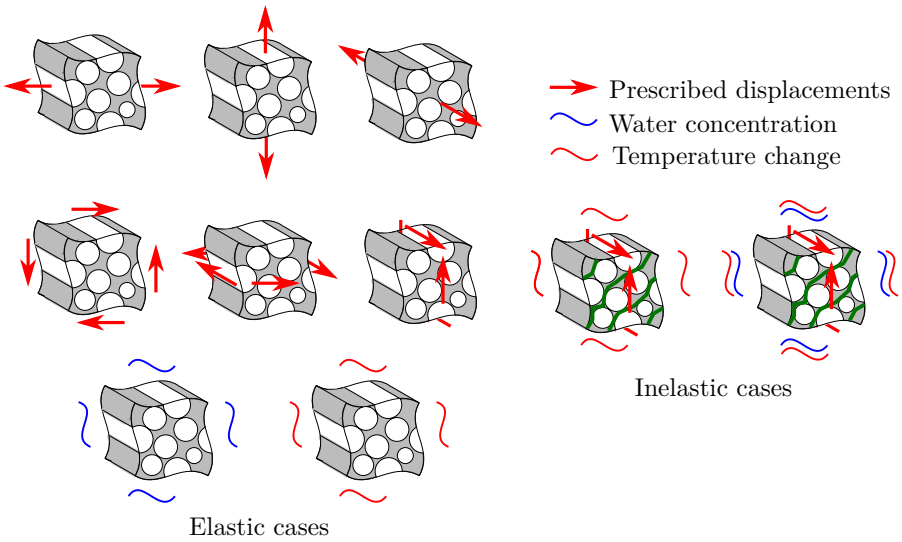

Figure 12: Load cases used for training the reduced-order model.

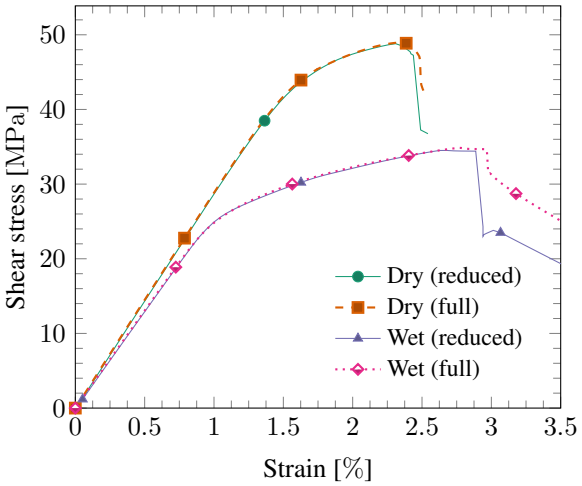

Figure 13: Reduced RVE model response for the inelastic training cases.

the dry test. Comparing the reduced internal force vectors for the POD-reduced and ECM-reduced models, the additional error caused by hyper-reduction is approximately $1.9\,\%$. The resultant speed-ups of the POD-reduced and ECM-reduced models with respect to the full-order model are 51 and 302, respectively.

Before using the reduced model in a multiscale analysis, it is interesting to assess its performance for non-trained load cases. Full and POD-reduced micromodels loaded in transverse shear at intermediate water concentration values are executed and their homogenized responses are compared in Fig. 14. The reduced model is capable of interpolating from the trained cases and correctly predicting material behavior for all concentration values, with only small overshoots in failure strain. The largest overshoot occurs for a concentration of $1.6\,\%$, a case that requires the largest amount of interpolation from either the dry or saturated states used for training. Influenced by the displacement modes at failure obtained from the training cases, failure strains are overestimated and steep load drops are obtained for all intermediate concentration values. It is interesting to note that, due to the smaller number of degrees of freedom, the reduced model features improved numerical robustness. This can be observed, for instance, in the $c = 2.4\,\%$ curve, a case on which the full analysis is terminated due to lack of convergence as soon as the softening branch of the equilibrium path is reached while the reduced model maintains the convergence behavior observed during the training cases.

For the next test, the POD-reduced model is assessed on its ability to represent loading at different strain rates. The full and reduced responses of a micromodel subjected to transverse shear at strain rates both 100 times faster and slower than the one used for training are shown in Fig. 15. In both cases, the reduced model correctly extrapolates the time-dependent material response in both the elastic and plastic regimes, while once again showing only a limited loss of accuracy in terms failure strain. As expected, the reduced model tends to exhibits behaviors closer to the ones used for training, leading to underestimated values of peak load and failure strain for the very fast strain rate and overestimated values for the very slow rate. For both studies on untrained load cases (water concentration and strain rate), the additional error caused by hyper-reduction (ECM), computed by comparing the norm of the reduced global internal force vectors with and without ECM, is at most $6\,\%$. Both the POD-reduced and the hyper-reduced models are therefore considered suitable for representing the full-order model, with significant acceleration and only limited loss of accuracy even upon considerable extrapolation from the load cases used in training.

A multiscale/multiphysics model of a three-point bending interlaminar shear test is performed.

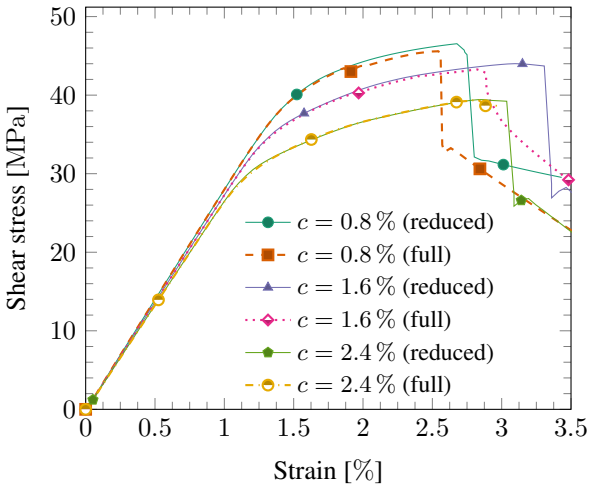

Figure 14: Reduced RVE model response for untrained scenarios of mechanical tests at different levels of saturation.

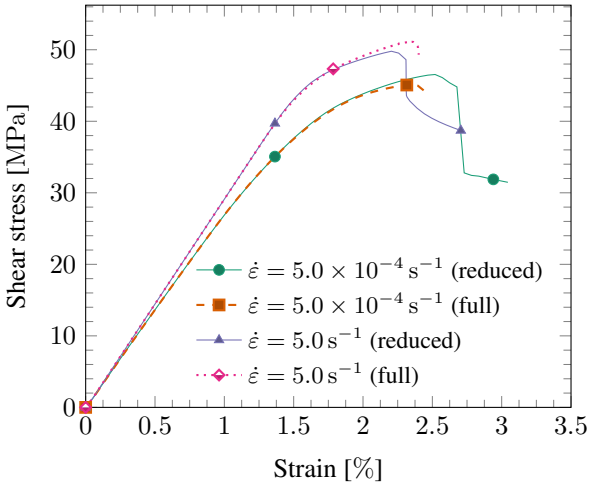

Figure 15: Reduced RVE model response for untrained scenarios of mechanical tests at different strain rates.

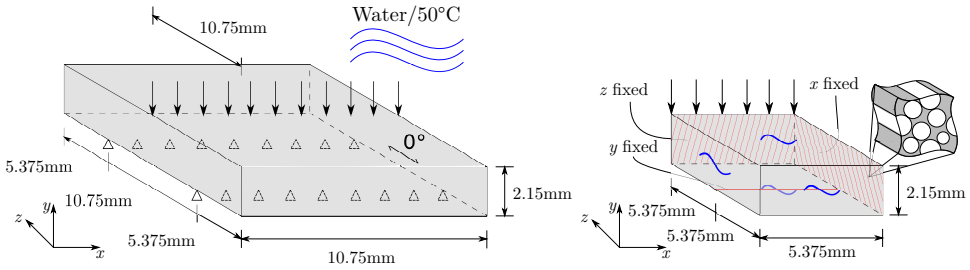

(a) Immersion problem (a) Modeling approach

Figure 16: Multiscale model of the aging and mechanical test of a short-beam specimen.

At the macroscale, symmetry along the x- and z-axes is exploited, and only one quarter of the short-beam is modeled (Fig. 16). The model is meshed with 8-node hexagonal elements. It is a known issue that an RVE ceases to exist upon microscopic strain localization, with the amount of energy dissipated by the macroscopic model being dependent on the size of the microdomain [37]. In order to bypass this issue, the thickness of a band of elements close to the specimen center along its thickness, where strain localization is expected, is made equal to the size of the micromodel [38]. The complete mesh comprises 1536 elements with a total of 5120 embedded micromodels. In order to further reduce computational effort, micromodels with a coarser mesh are used for material points located after the support along the length of the specimen, a region which is mostly free of stresses. The resultant mesh can be seen in Fig. 17. The analysis begins with a preconditioning phase with a time step $\Delta t = 25\,\mathrm{h}$, during which a constant water concentration of $3.2\,\%$ is applied at the boundary. After the immersion phase, the virtual specimen is cooled down from $50\,^{\circ}\mathrm{C}$ to $23\,^{\circ}\mathrm{C}$ at a rate of $5.5\,^{\circ}\mathrm{C\,min^{-1}}$, after which a mechanical test is performed in three-point bending at $1\,\mathrm{mm\,min^{-1}}$ and the resultant load, distributed over a length of $1.3\,\mathrm{mm}$, is used to compute the apparent interlaminar shear stresses using Eq. (4).

The multiscale model is used to obtain load-displacement curves for a dry specimen and specimens immersed for $250\,\mathrm{h}$, $500\,\mathrm{h}$ and $1000\,\mathrm{h}$, after which the water concentration field inside the specimen is non-homogeneous. In these situations, a stand-alone micromechanical analysis of the point of maximum concentration is not enough to derive the behavior of the macroscopic specimen, which is instead dictated by stress redistribution between regions with different water concentrations and suffers the influence of transient swelling stresses caused by the non-uniform concentration field.

Fig. 18 shows the obtained stress-displacement curves for each condition up until the point when interlaminar failure occurs at the center of the specimen. Although the mechanical response for the unaged sample is similar to the one obtained for a single RVE in pure transverse shear (Fig. 13), the same does not hold after aging. For an isolated micromodel saturated with water, failure occurs at approximately $34\,\mathrm{MPa}$, which is slightly higher but still reasonably close to the experimentally obtained strength (Fig. 4). On the other hand, the multiscale model points to a higher peak load of $39\,\mathrm{MPa}$ for the saturated specimen. This increase, which can only be captured in a multiscale analysis, results from the highly non-linear behavior of the saturated material prior to strain localization (Fig. 13), leading to stress redistribution along the specimen thickness. Predicting the interlaminar shear response of an aged specimen is therefore a more complex task than simply computing the micromechanical response of an isolated material point at its center.

Nevertheless, the gradual degradation behavior with water concentration observed in Fig. 4 is qualitatively reproduced by the multiscale model (Fig. 19). The numerically obtained peak stress for the unaged case is approximately $7\,\mathrm{MPa}$ lower than the average value obtained from the experiments. Since failure in the dry specimen is driven by resin fracture, such discrepancy is not sur-

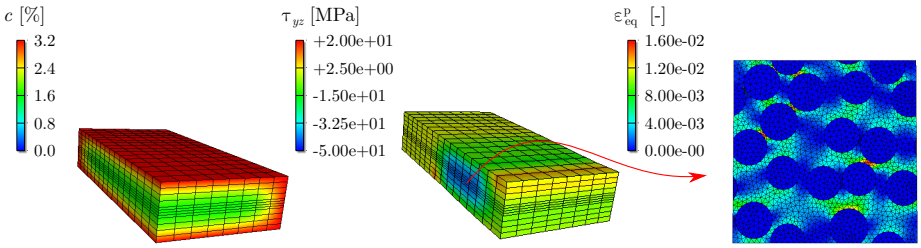

Figure 17: Snapshot of the multiscale analysis of a specimen immersed for 250 h at the onset of failure.

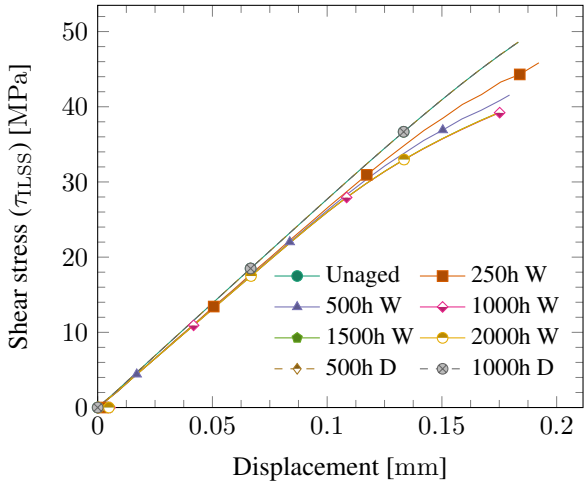

Figure 18: Numerically obtained ILSS stress-displacement curves.

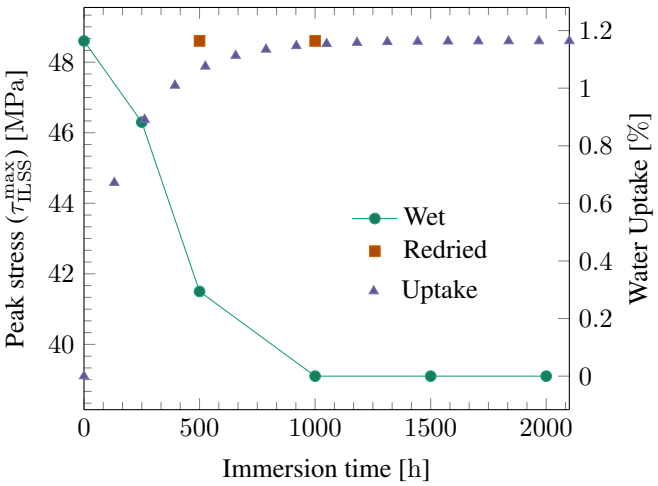

Figure 19: Numerical peak loads and water uptake for different immersion times.

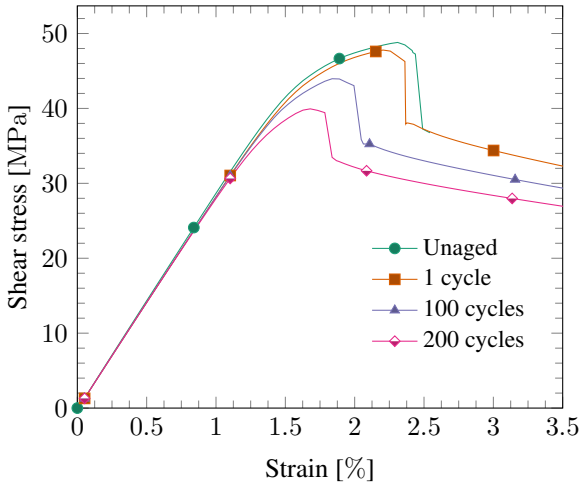

Figure 20: Reduced model response for testing after multiple immersion-redrying cycles.

prising given the fact that no reliable measurement for the fracture toughness of the present epoxy resin is currently available. Furthermore, the fiber bundles and resin-rich regions seen in Fig. 7 are not modeled, which would result in differences in crack propagation during the simulation. The high saturated peak stress levels predicted by the model suggest that interface degradation is significantly worse than the one used as input ($d_{\mathrm{w}}^{\infty} = 0.42$ from Table 4). This indicates that the saturated properties obtained through SFFT are overestimations of the actual degraded interface performance. Given the large measurement scatter obtained in those experiments (Section 2.3.1), the adopted values for X_{sh} and G_{IIc} are estimated with a high level of uncertainty.

Results on redried micromodels do not show any permanent degradation, with a peak stress of approximately $49\,\mathrm{MPa}$ being obtained for both unaged and redried specimens. This suggests that plastic deformations and interface debonding due to swelling are not responsible for the observed irreversible degradation, since the effect of swelling is already captured by the model. These results reinforce the hypothesis of chemical reactions permanently degrading interface performance, a mechanism also observed in the tomographic scans of Section 3. Including this effect in future iterations of the present framework is therefore interesting, either as an additional field problem by modeling the hydrolytic reaction or phenomenologically as a concentration threshold that assures a minimum level of degradation upon redrying.

As a last numerical example, it is interesting to take advantage of the computational efficiency of the reduced model in order to investigate the effect of cyclic immersion-redrying on the transverse shear strength of the composite material. For this example, the effect of cycling on a point close to the specimen surface is considered, for which complete saturation is supposed to be reached after $300\,\mathrm{s}$. For simplicity, the mechanical test is performed on the completely dry material (after cycling), eliminating the need for a concurrent multiscale approach.

Fig. 20 shows the model stress-strain response after 1, 100 and 200 immersion-drying cycles. Due to the viscous nature of the epoxy model and its dissipation-dependent fracture surface, and since saturation and redrying happen at relatively fast rates, cyclic differential swelling stresses promote a gradual strength decrease. Although it is reasonable to suppose the occurrence of such gradual degradation, further experimental evidence is required in order to confirm this trend.

5 Conclusions

This work presented a combined experimental and numerical study on hygrothermal aging of unidirectional glass/epoxy composites. Macroscopic material degradation was investigated through mechanical tests on short-beam specimens tested in three-point bending. Specimens were tested unaged, after having been immersed in water for various durations and after immersion-redrying cycles. Microscopic hygrothermal degradation was investigated through mechanical tests on single-fiber fragmentation specimens and by performing fractographic analyses on aged specimens through X-ray computed tomography. An attempt was made to numerically reproduce the observed degradation with a concurrent multiscale/multiphysics finite element model with hyper-reduced micromodels equipped with a viscous resin model and cohesive fiber-matrix interfaces with friction.

The mechanical properties of the fiber-matrix interface were estimated through a combination of single-fiber fragmentation tests and reverse modeling. Significant reductions in strength, friction and fracture toughness were observed after aging. However, the relatively low failure strain of the resin led to a large number of fragments for which no information could be extracted. Furthermore, the small number of valid fragments showed a large scatter in debonding behavior.

Results from interlaminar shear tests on specimens aged at $50\,^{\circ}\mathrm{C}$ showed a gradual strength decrease which had a strong correlation with the amount of water absorbed by the specimens. After saturation at $1000\,\mathrm{h}$ of immersion, the strength remained unchanged for another $1000\,\mathrm{h}$. Upon redrying, permanent degradation was observed for immersion times as short as $500\,\mathrm{h}$. Microscopic observations on these specimens through X-ray computed tomography revealed no signs of widespread interface debonding, in contrast with observations on specimens aged at $65\,^{\circ}\mathrm{C}$. It is concluded that an osmotic mechanism is activated at the higher temperature, leading to extensive debonding and additional water uptake. At $50\,^{\circ}\mathrm{C}$, it is hypothesized that diffusion and reaction are sufficiently slow as to allow the reaction products to leach out of the specimen before extensive osmosis occurs. In any case, these observations strongly suggest the occurrence of chemical damage at fiber-matrix interfaces.

The aging phenomenon was numerically simulated in a multiscale/multiphysics framework. A combination of the POD and ECM reduced-order modeling techniques was used to construct a reduced model which runs up to 300 times faster than the full-order one with limited loss of accuracy. The resultant model is able to qualitatively capture the experimentally observed dependency of interlaminar shear strength with water concentration, although uncertainties related to the fracture toughness of the resin and interface strength and toughness lead to incorrect predictions of both dry and saturated strengths.

Acknowledgements

The authors acknowledge the contribution of the TKI-WoZ (Grant number TKIW02005) and IRP-WIND projects for motivating and partly funding this research. The authors are grateful to Catharina Visser, Erik Vogeley, Frank Stroet, Koen Schellevis and Luc Smissaert for the assistance provided in the experimental part of this work.

References

References

[1] F. Naya, C. González, C. S. Lopes, S. van der Veen, F. Pons, Computational micromechanics of the transverse and shear behaviour of unidirectional fiber reinforced polymers including environmental effects, Compos Part A-Appl S.

[2] F. P. van der Meer, Micromechanical validation of a mesomodel for plasticity in composites, Eur J Mech A-Solid 60 (2016) 58–69.

[3] C. Qian, T. Westphal, R. P. L. Nijssen, Micro-mechanical fatigue modelling of unidirectional glass fibre reinforced polymer composites, Comput Mater Sci 69 (2013) 62–72.

[4] L. Gautier, B. Mortaigne, B. V., Interface damage study of hydrothermally aged glass-fibre-reinforced polyester composites, Compos Sci Technol 59 (1999) 2329–2337.

[5] G. M. Odegard, A. Bandyopadhyay, Physical aging of epoxy polymers and their composites, J Polym Sci Pol Phys 49 (2011) 1695–1716.

[6] R. Polanský, V. Mantlík, P. Prosr, J. Sušír, Influence of thermal treatment on the glass transition temperature of thermosetting epoxy laminate, Polym Test 28 (2009) 428–436.

[7] I. B. C. M. Rocha, S. Raijmaekers, R. P. L. Nijssen, F. P. van der Meer, L. J. Sluys, Hygrothermal ageing behaviour of a glass/epoxy composite used in wind turbine blades, Compos Struct 174 (2017) 110–122.

[8] F. Ellyin, C. Rorhbacher, Effect of aqueous environment and temperature on glass-fibre epoxy resin composites, J Reinf Plast Comp 19 (2000) 1405–1427.

[9] B. Dewimille, A. R. Bunsell, Accelerated ageing of a glass fibre-reinforced epoxy resin in water, Composites (1983) 35–40.

[10] M. C. Lafarie-Frenot, Damage mechanisms induced by cyclic ply-stresses in carbon-epoxy laminates: Environmental effects, Int J Fatigue 28 (2006) 1202–1216.

[11] M. Malmstein, A. R. Chambers, J. I. R. Blake, Hygrothermal ageing of plant oil based marine composites, Compos Struct 101 (2013) 138–143.

[12] A. Gagani, Y. Fan, A. H. Mulian, A. T. Echtermeyer, Micromechanical modeling of anisotropic water diffusion in glass fiber epoxy reinforced composites, J Compos Mater (2017) 1–15.

[13] Y. Joliff, W. Rekik, L. Belec, J. F. Chailan, Study of the moisture/stress effects on glass fibre/epoxy composite and the impact of the interphase area, Compos Struct 108 (2014) 876–885.

[14] A. Krairi, I. Doghri, A thermodynamically-based constitutive model for thermoplastic polymers coupling viscoelasticity, viscoplasticity and ductile damage, Int J Plas 60 (2014) 163–181.

[15] X. Poulain, A. A. Benzerga, R. K. Goldberg, Finite-strain elasto-viscoplastic behavior of an epoxy resin: Experiments and modeling in the glassy regime, Int J Plas 62 (2014) 138–161.

[16] B. F. Sørensen, Micromechanical model of the single fiber fragmentation test, Mech Mater 104 (2017) 38–48.

[17] C. Miehe, J. Schotte, J. Schröder, Computational micro-macro transitions and overall moduli in the analysis of polycrystals at large strains, Comput Mater Sci 16 (1999) 372–382.

[18] I. B. C. M. Rocha, F. P. van der Meer, R. P. L. Nijssen, L. J. Sluys, A multiscale and multiphysics numerical framework for modelling of hygrothermal ageing in laminated composites, Int J Numer Meth Eng 112 (2017) 360–379.

[19] K. Terada, M. Kurumatani, Two-scale diffusion-deformation coupling model for material deterioration involving micro-crack propagation, Int J Numer Meth Eng 83 (2010) 426–451.

[20] Z. Liu, M. Bessa, W. K. Liu, Self-consistent clustering analysis: An efficient multi-scale scheme for inelastic heterogeneous materials, Comput Method Appl M 306 (2016) 319–341.

[21] J. A. Hernández, M. A. Caicedo, A. Ferrer, Dimensional hyper-reduction of nonlinear finite element models via empirical cubature, Comput Method Appl M 313 (2017) 687–722.

[22] P. Kerfriden, O. Goury, T. Rabczuk, S. P. A. Bordas, A partitioned model order reduction approach to rationalise computational expenses in nonlinear fracture mechanics, Comput Method Appl M 256 (2013) 169–188.

[23] I. B. C. M. Rocha, F. P. van der Meer, S. Raijmaekers, F. Lahuerta, R. P. L. Nijssen, L. J. Sluys, Numerical/experimental study of the monotonic and cyclic viscoelastic/viscoplastic/fracture behavior of an epoxy resin, Under Review.

[24] I. B. C. M. Rocha, F. P. van der Meer, L. J. Sluys, Efficient micromechanical analysis of fiber-reinforced composites subjected to cyclic loading through time homogenization and reduced-order modeling, Under Review.

[25] ISO 14130 - Fibre-reinforced plastic composites - Determination of apparent interlaminar shear strength by short-beam method, Tech. rep., ISO (1997).

[26] B. W. Kim, J. A. Nairn, Observations of fiber fracture and interfacial debonding phenomena using the fragmentation test in single fiber composites, J Compos Mater 36 (2002) 1825–1858.

[27] U. A. Mortensen, T. L. Andersen, J. Christensen, M. A. M. Maduro, Experimental investigation of process induced strain during cure of epoxy using optical fiber bragg grating and dielectric analysis, in: In: Proceedings of the 18th European Conference on Composite Materials, 2018.

[28] F. P. van der Meer, S. Raijmaekers, I. B. C. M. Rocha, Interpreting the single fiber fragmentation test with numerical simulations, Under Review.

[29] L. P. Mikkelsen, [Dataset] A combined experimental/numerical investigation on hygrothermal aging of fiber-reinforced composites, Zenodo - `https://doi.org/10.5281/zenodo.1313247` (2018).

[30] A. Gagani, A. T. Echtermeyer, Fluid diffusion in cracked composite laminates - Analytical, numerical and experimental study, Compos Sci Technol 160 (2018) 86–96.

[31] A. Arefi, F. P. van der Meer, M. R. Forouzan, M. Silani, Formulation of a consistent pressure-dependent damage model with fracture energy as input, Compos Struct 201 (2018) 208–216.

[32] Z. P. Bažant, B. Oh, Crack band theory for fracture of concrete, Matériaux et Construction 16 (1983) 155–177.

[33] G. Alfano, E. Sacco, Combining interface damage and friction in a cohesive-zone model, Int J Numer Meth Eng 68 (2006) 542–582.

[34] I. B. C. M. Rocha, S. Raijmaekers, F. P. van der Meer, R. P. L. Nijssen, H. R. Fischer, L. J. Sluys, Combined experimental/numerical investigation of directional moisture diffusion in glass/epoxy composites, Compos Sci Technol 151 (2017) 16–24.

[35] P. Kerfriden, P. Gosselet, S. Adhikari, S. P. A. Bordas, Bridging proper orthogonal decomposition methods and augmented newton-krylov algorithms: An adaptive model order reduction for highly nonlinear mechanical problems, Comput Method Appl M 200 (2011) 850–866.

[36] Jive - Software development kit for advanced numerical simulations, http://jive.dynaflow.com, accessed: 04-03-2018.

[37] V. P. Nguyen, O. Lloberas Valls, M. Stroeven, L. J. Sluys, On the existence of representative volumes for softening quasi-brittle materials - a failure zone averaging scheme, Comput Method Appl M 199 (2010) 45–48.

[38] I. M. Gitman, H. Askes, L. J. Sluys, Coupled-volume multi-scale modelling of quasi-brittle material, Eur J Mech A-Solid 27 (2008) 302–327.